POLITECNICO DI TORINO
Repository ISTITUZIONALE

Facesheet Perforation Geometry Effects on Single-Degree-of-Freedom Acoustic Liners Impedance

Original
Facesheet Perforation Geometry Effects on Single-Degree-of-Freedom Acoustic Liners Impedance / Rossi, F., Bonomo, L., Cordioli, J., Avallone, F.. - In: AIAA JOURNAL. - ISSN 1533-385X. - (2026). [10.2514/1.J067300]

Availability:
This version is available at: 11583/3015342 since: 2026-09-10T12:56:54Z

Publisher:
American Institute of Aeronautics and Astronautics

Published
DOI:10.2514/1.J067300

Terms of use:

This article is made available under terms and conditions as specified in the corresponding bibliographic description in the repository

Publisher copyright
AIAA preprint/submitted version e/o postprint/Author's Accepted Manuscript

(Article begins on next page)

18 November 2026

Facesheet Perforation Geometry Effects on Single-Degree-of-Freedom Acoustic Liners Impedance*

Felipe R. Rossi†, Lucas A. Bonomo‡ and Julio A. Cordioli§
Federal University of Santa Catarina, Florianópolis - SC, 88040-900, Brazil

Francesco Avallone¶
Politecnico di Torino, 10129, Torino, Italy

I. Introduction

The treatment of the tonal component of fan noise in modern turbofan-powered aircraft remains a major aspect of the aircraft certification process. Since the early years of the turbofan era, acoustic liners installed in the nacelle have been the gold standard for tonal fan noise mitigation. The most typical acoustic liner design for turbofan applications, namely the Single-Degree-Of-Freedom (SDOF) liner, consists of a perforated facesheet backed by a honeycomb-like cavity structure, thus emulating an array of Helmholtz resonators. This configuration provides high attenuation over a narrow frequency band, which is usually tuned to match the fan Blade Passing Frequency (BPF) and its harmonics, corresponding to the dominant tonal-noise frequencies [1].

While the hole diameter in a liner perforated facesheet is on the order of millimeters, the nacelle dimensions (and the wavelengths of the dominant propagating modes) are on the order of meters. Therefore, it is still impractical to represent acoustic liners explicitly in acoustic numerical and/or analytical models [2]. The common approach is to represent the liner through its locally reactive, frequency-dependent complex acoustic impedance, $\tilde{Z}(\omega)$, which can then be used as a boundary condition in numerical and analytical models. The real component of the impedance is associated with dissipative mechanisms, which are usually related to the properties of the perforated facesheet. In contrast, the imaginary component, namely the reactance, is associated with stiffness and inertial effects and is governed by the combined contributions of the cavity depth and the facesheet mass reactance.

The impedance of acoustic liners is known to depend primarily on their geometry, but also on the operating conditions, namely the Sound Pressure Level (SPL), the grazing-flow velocity, and the boundary layer over the perforated facesheet [3, 4]. Given the complexity of this multiphysics problem, the determination of acoustic liner impedance is still primarily an experimental task, although high-fidelity numerical models are becoming a feasible alternative [2, 5]. Semi-empirical models have also been widely used to estimate the acoustic impedance, especially during the early stages of liner design [6]. A key aspect of these models is the assumption of sharp-edged holes in the perforated facesheet, i.e., perfectly cylindrical perforations. However, recent findings suggest that "imperfections" in the liner manufacturing process may lead to perforations that are not sharp-edged, which can strongly affect the impedance. A key experimental observation pointing to this issue is reported in Ref. [7], where 3D-printed liner samples with rounded perforation edges exhibited significantly lower resistance than that predicted by semi-empirical models. A numerical and experimental study supporting the conclusion that this behavior was caused by edge rounding is presented in Ref. [8], where a Normal Incidence Tube (NIT) configuration was used. Ref. [9] have studied the non-linear effects of multi-tone excitation using DNS models, considering possible orifice geometries. Even though the main object of the study was the multi-tone interactions, the results suggests a dependence on the impedance on the different geometries. To the best of the authors' knowledge, although studies investigating manufacturing-process effects are available in the literature [6], there is still no dedicated parametric experimental study on the effects of perforation-edge geometry on acoustic liner impedance in the presence of grazing flow. Therefore, there is still a gap in the literature regarding appropriate impedance models linked to manufacturing processes adopted (e.g. drilling, punching, grit blasting, resulting in varying hole shapes) and/or the manufacturing quality (e.g. adhesive blockage on the perforations, filleting, etc.).

*A preliminary version of this paper was presented as AIAA Paper 2026–3501 at the 32th AIAA/CEAS Aeroacoustics Conference in Brussels, Belgium.

†MSc Student, Department of Mechanical Engineering, felipe.rossi@lva.ufsc.br.

‡Aeroacoustics Researcher Fellow and Lecturer, Department of Mechanical Engineering, lucas.bonomo@lva.ufsc.br, AIAA Young Professional Member. Corresponding author.

§Associate Professor, Department of Mechanical Engineering, julio.cordioli@ufsc.br, AIAA Professional Member.

¶Full Professor, Departmento of Mechanical and Aerospace Engineering, francesco.avallone@polito.it, AIAA Professional Member.

This work addresses the lack of experimental data comparing acoustic liner impedance on the presence of grazing flow for different perforation shapes. Four liner samples were manufactured with the same nominal inner diameter (i.e., same open-area percentage), but with different hole's edge geometries, namely (i) sharp; (ii) outside chamfered; (iii) inside chamfered; and (iv) outside and inside chamfered. The acoustic liner impedance is assessed by means of two different experimental techniques at the Liner Impedance Test Rig of the Federal University of Santa Catarina (LITR/UFSC). The remainder of this document is structured as follows. Section II describes the liner samples and their geometrical characterization. Section III describes the experimental setup and test matrix. The results are presented and discussed in Section IV. Finally, the main conclusions are summarized in Section V.

II. Liner Samples

Given recent issues faced by the authors in ensuring quality and dimensional control when manufacturing 3D-printed liner samples[7], especially in the facesheet orifices, the liner samples in this work were machined from solid aluminum blocks using conventional manufacturing processes. Four different perforation configurations were considered: (I) a sharp-edged hole; (II) a hole with an outer chamfer; (III) a hole with an inner chamfer; and (IV) a hole chamfered on both sides. The corresponding configurations and geometric parameters of the samples are shown in Fig. 1, and the nominal values for all configurations are presented in Table 1. The facesheet thickness, $t = 0.635$ mm, is constant across all configurations. Additionally, since the inner hole diameter, $d_0 = 1.0$ mm, and the number of holes per cavity are kept constant, the nominal Percentage of Open Area (POA, or, σ_{d_0}) based on the inner diameter is also the same for all configurations.

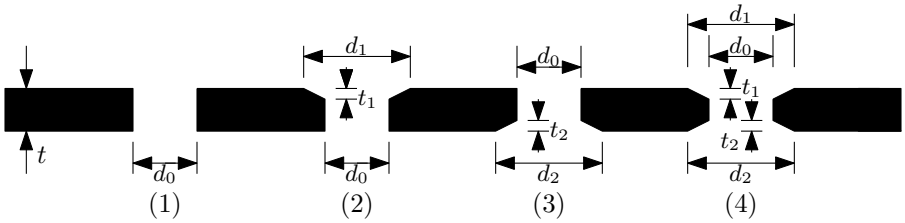


Fig. 1 Liner perforation geometries and parameters.

Table 1 Liner perforation parameters; all dimensions are in millimeters.

#	Geometry	Code	t	t_1	t_2	d_0	d_1	d_2
(1)	Sharp edged	SE	0.635	-	-	1.0	-	-
(2)	Outside Chamfered	OC	0.635	0.1	-	1.0	1.2	-
(3)	Internal Chamfered	IC	0.635	-	0.1	1.0	-	1.2
(4)	Both sides Chamfered	DC	0.635	0.1	0.1	1.0	1.2	1.2

The samples have overall dimensions of 210 mm in length and 150 mm in height. They are composed of chambers arranged in an 8×16 cell configuration, with each cell containing 8 holes and the cavity depth is $h = 38.1$ mm for all configurations. The individual cell chambers have dimensions of 9.9×9.9 mm^2, with fillets of 2 mm radius at the corners to facilitate manufacturing. Hence, each cell has a POA of approximately 6.4 %, while the overall samples has $\sigma_{d_0} = 3.83$ %. Although σ_{d_0} based on the inner diameter is kept constant, the surface porosity changes, considering that the external diameter changes with the chamfering. For this case, we use a new quantity σ_{d_1} which is an equivalent POA, but considering the external diameter for the open-area evaluation. Therefore, the sample with outside chamfers (OC and DC) have $\sigma_{d_1} = 5.51$ %.

Manufacturing limitations were imposed by the cutting tool required to produce the chamfers, which meant that the samples with chamfers facing the cavity interior could not be manufactured as a single piece. Therefore, while SE and OC were machined from a single block with depth $t + h = 38.735$ mm, IC and DC were manufactured in two pieces, such that most of the core was separated into an isolated part. More precisely, these samples were split at 8.5 mm from the facesheet, resulting in one piece with a depth of 8.5 mm (the facesheet and a small portion of the core) and another piece with a depth of 30.235 mm (the remaining portion of the cavity core). The two manufacturing approaches are

illustrated in Fig. 2. Finally, to close the back of the open cavities, a thick acrylic plate was used as the back plate for the samples and was clamped only during testing.

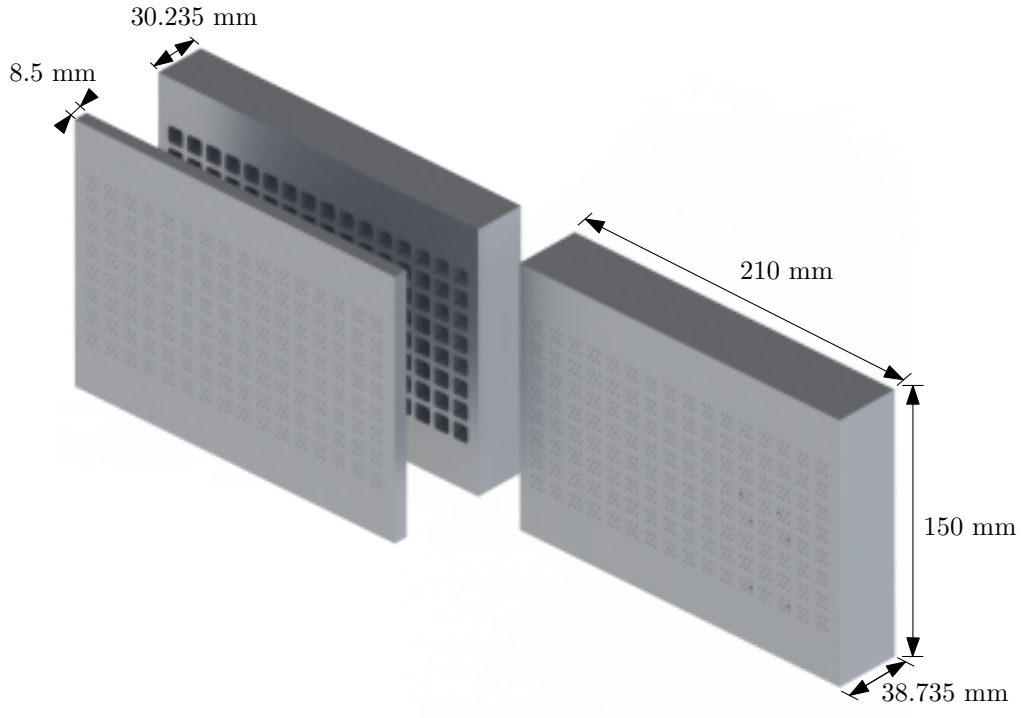


Fig. 2 Illustration of the liner samples. On the left, the sliced method for configurations (III) and (IV); on the right, the single piece method for configurations (I) and (II).

A. Geometric Optical Characterization

An optical analysis was carried out using a stereoscope to assess the actual geometry resulting from the manufacturing process. A Zeiss Stemi SV8 stereoscope equipped with a Leica camera was used, allowing the acquisition of high-resolution images. Pixel-counting methods were then applied using the software supplied by the stereoscope manufacturer.

The procedure used to obtain the perforation parameters consisted of randomly selecting 15 holes from each sample and measuring the following dimensions: (i) the external diameter, defined either as the largest chamfer diameter or as the diameter at the facesheet wall (d_1 or d_2), and (ii) the internal diameter, defined as the diameter at the midpoint of the hole, which should correspond to the smallest diameter (d_0). For the sharp-edged geometry, the internal and external diameters were assumed to be identical. For the samples manufactured in two pieces (configurations (III) and (IV)), it was also possible to obtain measurements of the internal diameter d_0 from the inner side of the liner. Afterwards, the average and standard deviation of each parameter were evaluated. The statistics obtained for all configurations and measured parameters are presented in Table 2.

It was observed that, for all chamfered configurations, the average internal diameter d_0 was smaller than the nominal value. This can be explained by the formation of small burrs during chamfer machining, which may have locally reduced the inner diameter of the orifice. Based on the semi-empirical model from Ref. [4], for the frequency and velocity ranges covered in this work (to be detailed in Section III.D), these small variations in the inner diameter may lead to variations in the normalized liner resistance smaller than 0.07 in the absence of flow, and smaller than 0.13 for the case with the maximum flow speed considered in this work, at 145 dB. Nonetheless, the external chamfer diameters were always larger than the nominal values, while remaining within manufacturing tolerances. Finally, the dimensional variation observed in the measurements was considered satisfactorily small.

Table 2 Statistical data from the geometric optical characterization of the samples. All dimensions are in millimeters.

Parameter	Nominal value	Average	Standard deviation
(I) Sharp Edged - SE			
d_0	1.0	1.000	0.006
(II) Outside Chamfered - OC			
d_0	1.0	0.966	0.006
d_1	1.2	1.294	0.017
(III) Inside Chamfered - IC			
$d_0\|_{\text{out}}$	1.0	1.010	0.009
$d_0\|_{\text{in}}$	1.0	0.982	0.013
d_2	1.2	1.242	0.011
(IV) Both sides Chamfered - DC			
$d_0\|_{\text{out}}$	1.0	0.990	0.009
d_1	1.2	1.273	0.018
$d_0\|_{\text{in}}$	1.0	0.984	0.011
d_2	1.2	1.258	0.013

B. Goodrich Liner Impedance Semi-empirical Model

To complement the experimental observations and gain deeper physical insight into the acoustic behavior of the chamfered configurations, the semi-empirical Goodrich model for SDOF liners is employed [4]. This analytical framework provides a valuable reference to decouple the effects of nominal perforation geometry from those introduced by variations in effective surface area.

Details regarding the implementation of this model, including the correction for cavity width and partition wall blockage effects via the Zwikker-–Kosten transmission line approach, can be found in Ref. [7]. The liner impedances were estimated using two parameter sets: one based on the nominal internal hole diameter (d_0 and σ_{d_0}), and another considering the expanded surface opening (d_1 and σ_{d_1}). Evaluating these theoretical estimates alongside experimental data allows for a clearer distinction between pure porosity expansion effects and edge-induced fluid dynamic behavior.

III. Experimental Setup

This section presents a brief description of the experimental facilities and methods used in this work. For further details, the reader is referred to a previous publication by the authors, Ref. [10], in which both the facilities and the methods are discussed in detail.

A. Test Facilities

In this work, the LITR/UFSC was used to measure the acoustic impedance of the liner samples. The LITR/UFSC test rig consists of a modular waveguide with a rectangular cross-section. The internal duct has a width of $W = 40\,\text{mm}$ and a height of $H = 100\,\text{mm}$. The central section is the liner sample holder, which accommodates liner samples with lengths of up to $L_{\text{liner, max.}} = 420\,\text{mm}$.

Flow is provided by a compressed-air system, which can sustain a bulk Mach number corresponding to approximately $M_{\text{max.}} \approx 0.6$. The flow velocity and temperature are measured in real time by means of a Pitot tube and a thermoresistance located immediately upstream of the test section. Loudspeakers, installed both upstream and downstream of the liner sample holder, allow for the generation of acoustic waves propagating with and against the flow, respectively. The current setup allows pure-tone acoustic waves propagating toward the liner at SPLs of up to approximately 150 dB over the frequency range from 0.5 kHz to 6.0 kHz. Flush-mounted microphones are installed on the wall opposite the liner, both upstream and downstream of the liner sample. In addition, an array of equally spaced flush-mounted microphones is installed on the wall facing the lined section, allowing the use of Prony-based eduction methods.

B. Inverse Impedance Eduction

For the purposes of this work, the acoustic propagation problem is simplified to a two-dimensional duct, as depicted in Fig. 3. Assuming a positive uniform parallel flow in the axial direction (z), with time-harmonic and axially harmonic acoustic pressure perturbations, i.e., $\tilde{p} \propto \exp(\mathrm{i}\omega t - \mathrm{i}k_z z)$, the acoustic field is governed by the Convected Helmholtz Equation,

$$\left(\nabla_\perp^2 + (k - Mk_z)^2 - k_z^2\right)\tilde{p} = 0, \tag{1}$$

where $M \equiv U/c_0$ is the bulk Mach number, c_0 is the speed of sound, $k = \omega/c_0$ is the free-field wavenumber, and k_z is the axial wavenumber. In this work, under the two-dimensional duct assumption, $\nabla_\perp^2 \equiv \frac{\mathrm{d}^2}{\mathrm{d}x^2}$.

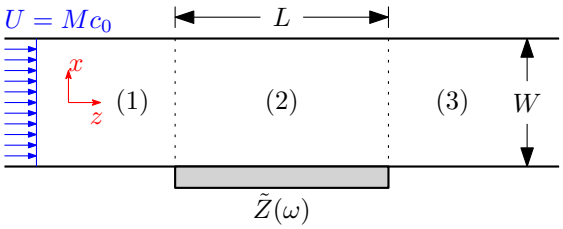


Fig. 3 Two-dimensional waveguide and coordinate system adopted in this work.

At each section j, the acoustic field $\tilde{p}(x, z)$ can be approximated by a sum of $\mathcal{N}$ acoustic modes,

$$\tilde{p}^{(j)}(x, z) = \sum_{n=1}^{\mathcal{N}} \left(A_n^{(j)+}\psi_n^{(j)+}(x)\exp\left(-\mathrm{i}k_{z,n}^{(j)+}z\right) + A_n^{(j)-}\psi_n^{(j)-}(x)\exp\left(-\mathrm{i}k_{z,n}^{(j)-}z\right)\right), \tag{2}$$

where A_n are the modal amplitudes, $\psi_n(x)$ are the mode shapes, and the superscripts + and − denote downstream- and upstream-propagating modes, respectively.

At the majority of the duct walls, the rigid wall boundary condition implies $\frac{\mathrm{d}\hat{p}}{\mathrm{d}x} = 0$. On the other hand, at the lined wall, the Ingard–Myers Boundary Condition (IMDC) [11, 12] is assumed,

$$\frac{\mathrm{d}\tilde{p}}{\mathrm{d}x} = \frac{\mathrm{i}}{k\tilde{Z}}(k - Mk_z)^2\tilde{p}. \tag{3}$$

For the frequency range and microphone locations considered here, the modal amplitudes in the rigid-walled sections can be determined by means of a plane-wave decomposition. This can be carried out using an overdetermined decomposition procedure, for example, in the upstream section,

$$\begin{bmatrix} \exp\left(-\mathrm{i}k_{z,1}^{+}z_1\right) & \exp\left(-\mathrm{i}k_{z,1}^{-}z_1\right) \\ \exp\left(-\mathrm{i}k_{z,1}^{+}z_2\right) & \exp\left(-\mathrm{i}k_{z,1}^{-}z_2\right) \\ \exp\left(-\mathrm{i}k_{z,1}^{+}z_3\right) & \exp\left(-\mathrm{i}k_{z,1}^{-}z_3\right) \\ \exp\left(-\mathrm{i}k_{z,1}^{+}z_4\right) & \exp\left(-\mathrm{i}k_{z,1}^{-}z_4\right) \end{bmatrix} \begin{bmatrix} A_1^{+} \\ A_1^{-} \end{bmatrix} = \begin{bmatrix} \tilde{p}_1 \\ \tilde{p}_2 \\ \tilde{p}_3 \\ \tilde{p}_4 \end{bmatrix}, \tag{4}$$

and similarly for the downstream section. The plane-wave axial wavenumber, $k_{z,1}^{\pm} = \pm kK_0/(1 \pm K_0 M)$, also accounts for viscothermal losses at the duct walls through the first-order Kirchhoff solution K_0 [13]. Afterwards, the modal amplitudes in the lined section can be determined by enforcing continuity of mass and momentum at each interface, following Ref. [14]. This procedure is known in the literature as the Mode Matching Method (MMM).

The lined-wall impedance is obtained through an iterative procedure. An initial impedance guess $\tilde{Z}_i$is required to compute the theoretical acoustic field p_q^{num} at each microphone location z_q, which is then compared with the measured acoustic field p_q^{exp} by means of the following cost function

$$\mathcal{F}(\tilde{Z}) = \sum_{q=1}^{Q} \left| \frac{\tilde{p}_q^{\mathrm{exp}} - \tilde{p}_q^{\mathrm{num}}(\tilde{Z})}{\tilde{p}_q^{\mathrm{exp}}} \right|, \tag{5}$$

where $Q = 8$ is the total number of microphones. The Levenberg–Marquadt algorithm [15, 16] is used to minimize this cost function, yielding the liner impedance. In order to accelerate convergence, the semi-empirical impedance model from Ref. [4] is employed as the initial guess for the liner impedance.

C. In-Situ Technique

The in-situ measurement technique estimates the acoustic liner impedance from measurements of the acoustic pressure at the facesheet and at the rigid backing plate of a liner cell. The in-situ technique implicitly assumes that the liner is locally reactive, and no assumptions are made regarding the flow outside the liner. Therefore, it does not rely on the definition of a boundary condition such as the Ingard–Myers boundary condition [11, 12], since it does not attempt to model the acoustic field as in impedance-eduction techniques.

The main assumptions of the in-situ technique are that: (i) the backplate is perfectly reflective; (ii) only standing plane waves exist in the cell; and (iii) the facesheet is acoustically thin, so that the acoustic particle velocity is the same on both sides of the facesheet [17]. Under these conditions, it can be shown that the in-situ impedance is given by

$$\tilde{Z} = \frac{-\mathrm{i}\tilde{H}_{\mathrm{fb}}}{\sin(kh)}, \tag{6}$$

where $\tilde{H}_{\mathrm{fb}}$ is the ratio between the complex acoustic pressures at the facesheet and the backplate, and h is the cavity height. In practice, $\tilde{H}_{\mathrm{fb}}$ is determined from the transfer function between the complex acoustic pressures at the facesheet and the backplate. In this work, the capillary-probe approach described in Ref. [10], based on the earlier work from Ref. [18], is used. The effect of the instrumentation on the measured impedance is corrected using

$$\tilde{Z}_{\mathrm{liner}} = \frac{\tilde{Z}_{\mathrm{meas}} + \mathrm{i}\cot(kh)}{1 - \varepsilon_w - \varepsilon_m} + \mathrm{i}\frac{\varepsilon_m}{\tan(kh)} - \mathrm{i}\cot(kh). \tag{7}$$

where $\tilde{Z}_{\mathrm{meas}}$ is the measured impedance obtained from Eq. (6); ε_w is the ratio between half of the cross-sectional area of the surrounding cell walls and the area of the liner cell; and ε_m is the ratio between the blocked volume due to instrumentation and the cell volume.

D. Test Matrix

In this work, the flow conditions are defined in terms of the centerline Mach number, M_{c}, which corresponds to the maximum flow velocity in the duct cross-section. Three flow conditions are considered: (i) the no-flow case, $M_{\mathrm{c}} = 0.00$; (ii) $M_{\mathrm{c}} = 0.32$; and (iii) $M_{\mathrm{c}} = 0.50$, which correspond to bulk Mach numbers of $M = 0.000$, 0.272, and 0.436, respectively.

The acoustic excitation consisted of a pure-tone signal ranging from 500 Hz to 3000 Hz in 100 Hz increments. The acoustic source was positioned either upstream or downstream of the liner, with only one propagation direction considered at a time. The SPL was defined based on the amplitude of the plane wave propagating toward the liner, and the source power was adjusted such that the SPL was either 130 dB or 145 dB for the cases with $M_{\mathrm{c}} = 0.00$ and $M_{\mathrm{c}} = 0.32$, and 145 dB for the case with $M_{\mathrm{c}} = 0.50$, in order to ensure adequate signal-to-noise ratio under the highest-flow condition.

The impedance-eduction method was applied to all operating conditions and perforation configurations. However, the instrumentation of the sliced samples (IC and DC) was found to be nontrivial, making it difficult to ensure proper probe alignment and sealing. Therefore, the in-situ technique was applied only to the SE and OC configurations. Moreover, recent findings from high-fidelity numerical simulations of acoustic liners suggest that the impedance measured using the in-situ technique is strongly dependent on facesheet-probe positioning. Therefore, in this work, two adjacent cells were instrumented. These cells are located in the third column and in the middle rows of the sample. In one of them, the additional hole for the facesheet probe was positioned upstream of the cavity holes, whereas in the other it was positioned downstream of them, as schematically depicted in Fig. 4. The impedance obtained for both cavities was then averaged to obtain the final result. Furthermore, the samples were rotated between measurements with upstream and downstream source excitation, so that the instrumented cell was always located at the sample edge nearest to the acoustic source.

IV. Results and Discussion

The reader may have noticed that the test matrix of this study is substantially large. However, the main conclusions can be drawn from a much smaller subset of cases. Therefore, for the sake of brevity, only a representative set of results is presented in this document, while the complete dataset will be made publicly available in an open-source format. Unless otherwise stated, the results shown in the remainder of this document correspond to the upstream acoustic source configuration, which provides the clearest comparison between configurations. The results obtained with the

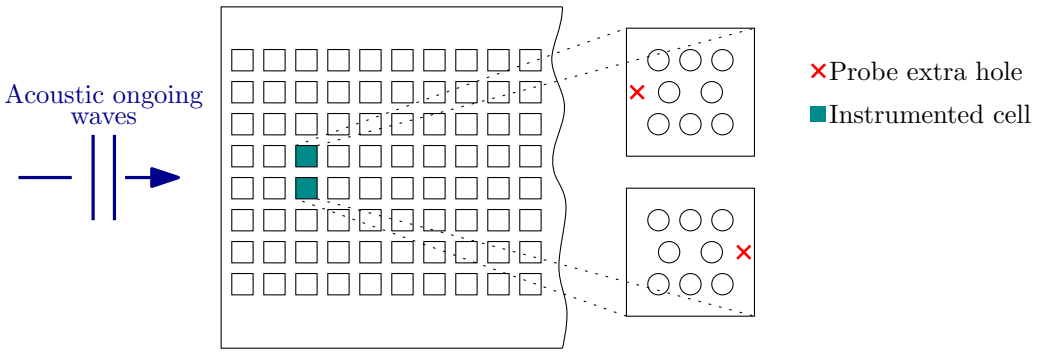


Fig. 4 Representation of the location of the instrumented cells for the in-situ technique and the facesheet-probe hole location.

opposite source arrangement were found to be qualitatively consistent with the same trends. In addition, for the inverse impedance-eduction method, only the cases with $M_c = 0.00$ and $M_c = 0.32$ are considered, since the accuracy of the assumed IMBC decreases significantly for $M_c = 0.50$ [19, 20]

First, the results obtained with the inverse impedance-eduction method are analyzed. Fig. 5 shows the results obtained for the no-flow case at both 130 dB and 145 dB, for all configurations. The results suggest that, as expected, in the absence of mean flow, the reactance is not significantly affected by the different perforation configurations, as the reactive behavior is primarily driven by the backing cavity geometry. At 130 dB, all configurations still show broadly similar resistance levels, although a slightly lower resistance is already observed for the both-sides chamfered (DC) configuration. This indicates that the sensitivity of acoustic liner resistance to perforation-edge shape is already present under no-flow conditions at 130 dB, in agreement with previous observations reported in Ref. [8], but remains substantially weaker than that observed at 145 dB.

On the other hand, the results obtained at 145 dB suggest a strong dependence on perforation-edge shape when nonlinear effects become relevant, in agreement with previous reports in the literature [8]. This pattern is especially clear in the mid-frequency range (1500 Hz $< f <$ 2500 Hz), where the resistance levels can be ordered as SE>OC>IC>DC. Also, the resistance decreases as the number of sharp edges explicitly decreases. This suggests that the acoustic viscous dissipation during the inflow and outflow stages at the liner orifices is strongly affected by perforation-edge geometry. One possible explanation is the increase in the discharge coefficient associated with the presence of chamfers.

One may notice that, at the lower-frequency end, the IC configuration displays a higher resistance than the OC configuration, whereas the opposite occurs above 1500 Hz. A key feature contributing to this crossover is a localized drop in resistance observed around 1500 Hz exclusively in the IC and DC configurations. Because this sharp reduction is uniquely shared by IC and DC, it strongly implicates the internal chamfer geometry. As a working hypothesis, this behavior is attributed to the rapid acoustic phase shift across the fundamental liner resonance (around 1400 Hz), which alters the phase relation between the cavity pressure and the acoustic particle velocity through the orifice. This phase inversion modifies the fluid coupling and vortex shedding dynamics specifically at the internal orifice edge during the acoustic cycle. Nevertheless, high-fidelity numerical simulations are required to confirm this hypothesis.

Furthermore, the semi-empirical model predictions for both the baseline (σ_{d_0}) and the increased external porosity (σ_{d_1}) are included in Fig. 5 for comparison. While the model captures the overall reactance trends accurately, the resistance predictions slightly overestimate the nonlinear behavior at 145 dB near the resonance frequency. Nevertheless, the model correctly anticipates that an increase in the effective surface porosity (from σ_{d_0} to σ_{d_1}) leads to a reduction in the acoustic resistance. This theoretical trend is qualitatively consistent with the experimental observations, where the chamfered configurations exhibit lower resistance than the sharp-edged baseline. However, at this stage, it is not possible to decouple the effects of the increased external porosity from the purely acoustic effects of the chamfer geometry. It is also worth noting that the model predictions (σ_{d_0} and σ_{d_1}) fail to reproduce the overall frequency-dependent behavior of the resistance, which is expected given that the model parameters were calibrated against in-situ data.

Fig. 6 displays the results obtained for a flow condition with $M_c = 0.32$, for all perforation configurations and both SPLs considered. The results suggest that, as in the no-flow case, the perforation-edge geometry has no significant effect on the reactance, although small differences are observed at the lower-frequency and high-frequency ends for the configurations with internal chamfering (IC and DC).

In the presence of grazing flow, the educed impedances are not significantly influenced by SPL-induced nonlinear

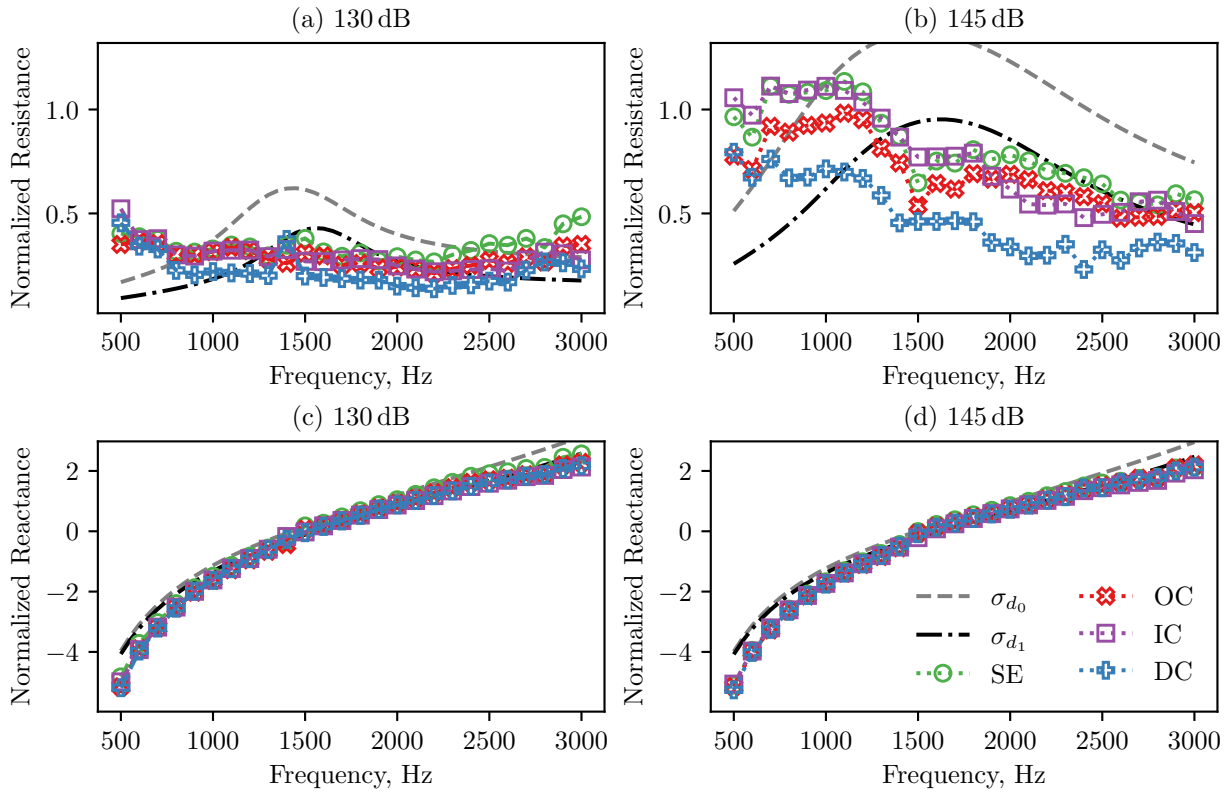


Fig. 5 Impedances educed with M_c = 0.00. Dashed and dot-dashed lines with no markers represents the impedances estimated with the semi-empirical model.

effects, in agreement with previous findings reported in Ref. [21], since the grazing flow induced resistance becomes dominant. A clear reduction in resistance associated with the presence of an outer chamfer at the facesheet holes is observed, as indicated by the significantly lower resistance values obtained for the OC and DC cases. Furthermore, the inner chamfer also appears to contribute to a reduction in liner resistance, since the DC and IC cases exhibit lower resistance than their corresponding counterparts with only an outer chamfer or no chamfer, namely OC and SE, respectively.

Regarding reactance (Figs. 6c and 6d), a subtle reduction is noticeable at higher frequencies ($f \gtrsim 2500$ Hz) for the chamfered configurations, most prominently in the IC and DC cases. This trend suggests that internal chamfering could induce a more pronounced reactance decrease at frequencies beyond the measured range (> 3 kHz), which might offer potential benefits for broadband noise attenuation by favorably modifying the effective end-correction. However, it must be emphasized that this remains a preliminary hypothesis, and further experimental work extended to higher frequencies is required to confirm this behavior.

To further investigate whether the reduction in grazing flow resistance for the chamfered configurations is a direct aerodynamic consequence of the edge shape or simply an effect of the increased effective surface porosity, the experimental results are compared against the Goodrich semi-empirical model predictions in Fig. 6. The model computed with the baseline porosity (σ_{d_0}) shows an excellent agreement with the SE configuration data. The model is computed using the larger external porosity (σ_{d_1}) associated with the chamfers, the predicted resistance drops and aligns reasonably well with the OC configuration data. While this agreement suggests that the reduction in liner resistance could be primarily driven by the increase in the effective open area exposed to the flow (σ_{d_1}), one cannot rule out that this might be a coincidental result. The current experimental dataset does not allow for a definitive isolation of the porosity effect from the complex flow shedding alterations caused by the chamfer profile itself.

To provide a clearer perspective on these relative differences, Fig. 7 presents the measured resistance ratios of the chamfered configurations (OC, IC, and DC) normalized by the SE baseline resistance [4]. The theoretical ratio predicted by the semi-empirical model, obtained by dividing the resistance calculated with σ_{d_1} by the one calculated with σ_{d_0}, is

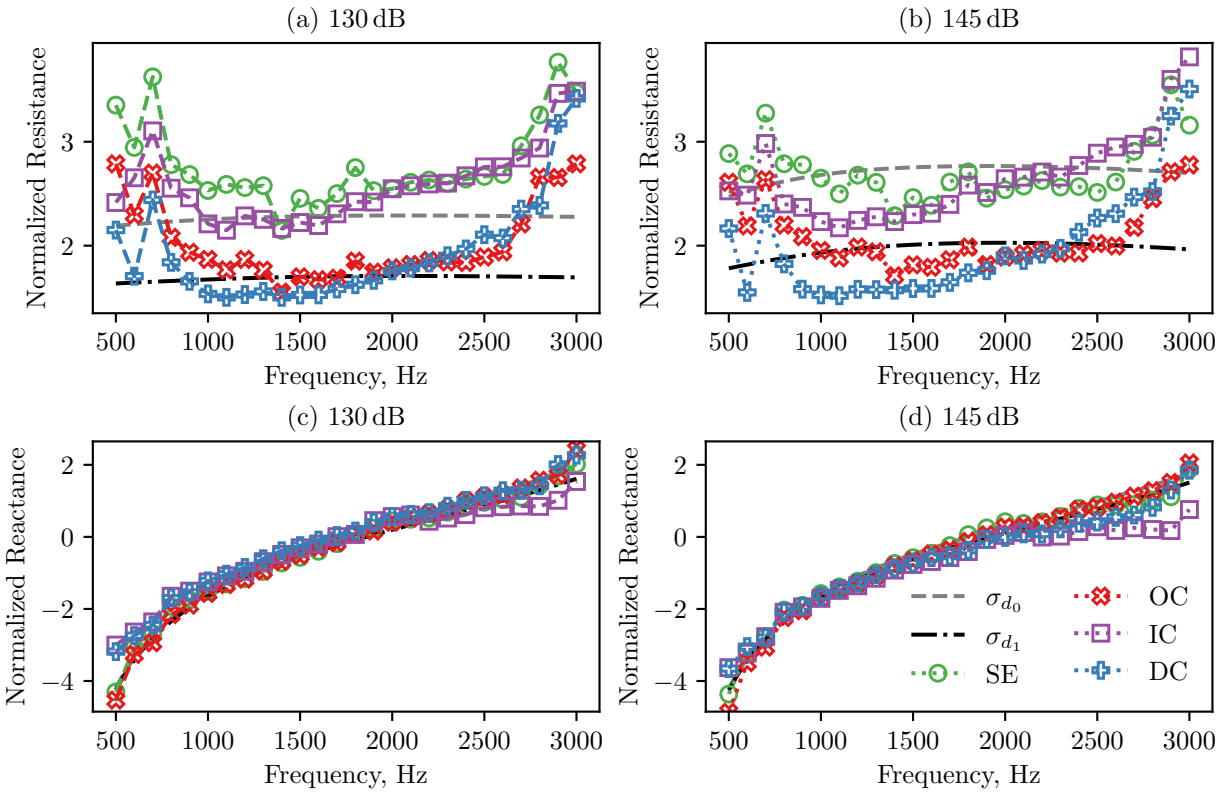


Fig. 6 Impedances educed with M_c = 0.32. Dashed and dot-dashed lines with no markers represents the impedances estimated with the semi-empirical model.

also included for comparison.

Under high-excitation no-flow conditions (145 dB, Fig. 7b), the localized drop in resistance just above 1500 Hz associated with the internal chamfering (IC and DC configurations) remains pronounced in these normalized ratios. On the other hand, under grazing flow conditions (Figs. 7c and 7d), the experimental resistance ratio for the OC configuration closely tracks the theoretical model ratio. This provides a quantitative backing to the hypothesis that the resistance drop for the OC sample scales well with the increased external porosity. From a fluid dynamic perspective, the enlarged opening on the flow-exposed side may shift the location of vortex shedding from the original orifice edge to the outer lip of the chamfer, causing the grazing flow to primarily interact with the larger external perimeter. Note that this behavior is likely sensitive to the chamfer angle and could similarly manifest in rounded edge geometries, for instance. However, as previously emphasized, while the deltas match the porosity correction, it remains uncertain whether this is a direct physical consequence of the enlarged open area or a coincidental aerodynamic effect introduced by the chamfer geometry.

Finally, the results obtained with the in-situ technique are presented in Fig. 8, allowing the analysis to be extended to higher mean-flow velocities. These results confirm the main trends observed in the impedance-eduction results: (i) the nonlinear effects induced by grazing flow dominate over those associated with SPL; (ii) the reactance is not significantly affected by the presence of chamfers at the perforation edges; and (iii) the presence of an outer chamfer significantly reduces the nonlinear increase in liner resistance associated with grazing flow.

In addition to the resistive drop, increasing the effective POA is theoretically expected to reduce the facesheet mass reactance, thereby shifting the liner resonance (approximated by the zero-crossing reactance) to a slightly higher frequency. The semi-empirical model captures this behavior, predicting an upward shift in the resonance frequency ranging from approximately 110 Hz to 130 Hz when moving from the baseline σ_{d_0} to the increased porosity σ_{d_1}. As accurately noted, the experimental reactance data obtained *in-situ* (Fig. 8) confirms this physical trend. Linear interpolation of the zero-crossing frequencies reveals that the outside-chamfered (OC) configuration exhibits an upward resonance shift ranging broadly from approximately 10 Hz to 270 Hz compared to the SE baseline, depending on the

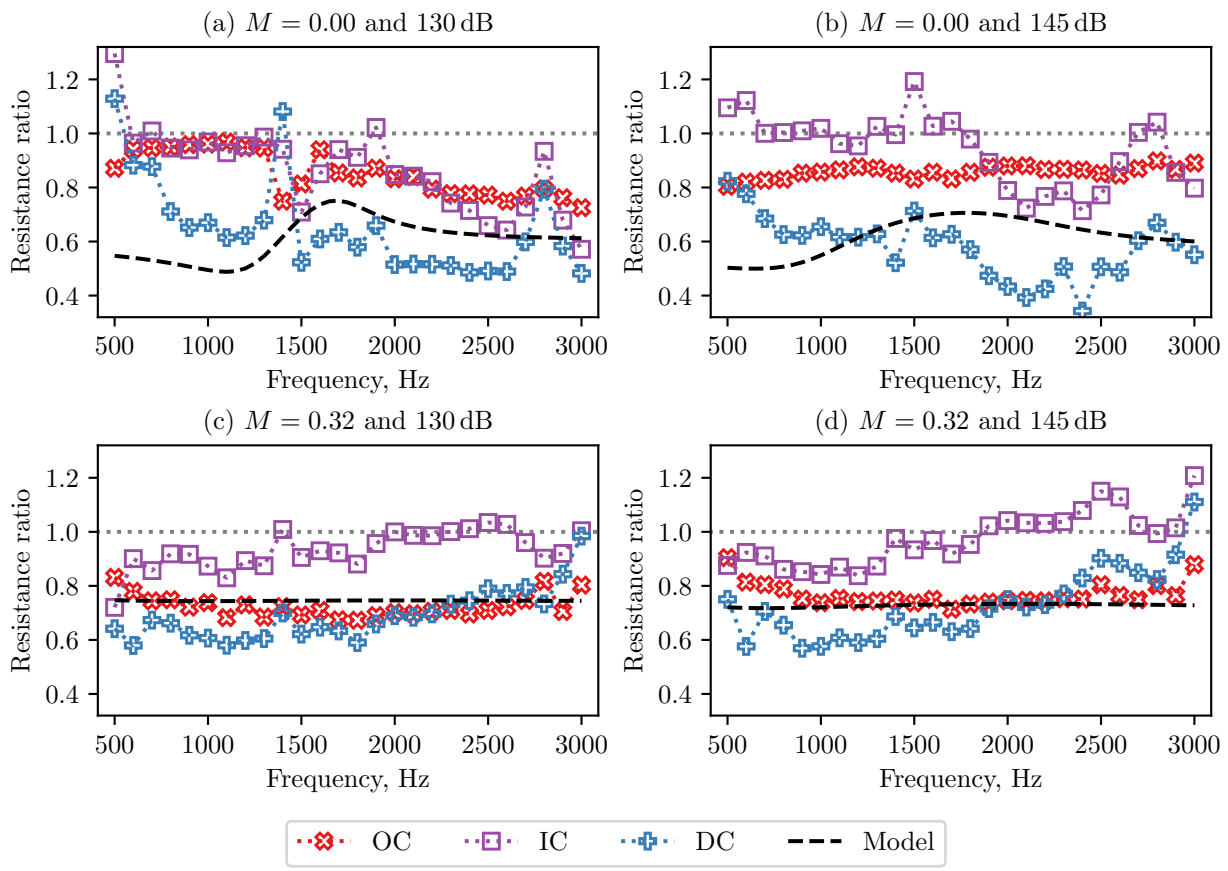


Fig. 7 Resistance ratios for different hole geometries (OC, IC, and DC) relative to the SE reference. The semi-empirical model ratio (σ_{d_1} over σ_{d_0}) is included for comparison.

SPL and grazing flow conditions. However, this large variance, coupled with the 100 Hz frequency step resolution adopted in the current experimental campaign, hinders a definitive quantitative characterization of this phase shift. Nonetheless, both the resistance drop and the consistently higher resonant frequencies observed in the experimental data remain physically consistent with the hypothesis of an effectively larger open area.

Furthermore, it is worth noting that the chamfered geometries inherently alter the effective thickness-to-diameter (t/d) ratio of the perforations. While defining a single effective t/d is non-trivial since the internal throat diameter (d_0) remains constant across all samples, the chamfering process effectively reduces the length of the straight cylindrical segment (lowering the effective t) and increases the average hole diameter (raising the effective d). This combined geometric effect decreases the overall effective t/d ratio, thereby contributing to the reduction of the linear viscous resistance of the facesheet, which aligns with the lower resistance values observed for the chamfered configurations. Recent numerical investigations on SDOF facesheet orifices [8] demonstrate that orifice edge geometry directly dictates the extent of flow separation and the resulting *vena contracta* effect. While sharp edges promote boundary layer detachment and higher acoustic resistance, chamfered edges alleviate flow contraction during the inflow phase, providing a clear fluid-dynamic basis for the resistance reductions observed in our experimental data.

V. Concluding Remarks

The effects of perforation-edge geometry on the impedance of SDOF acoustic liners were investigated. Four different configurations were considered, namely sharp-edged (SE), outside-chamfered (OC), internally chamfered (IC), and both-sides chamfered (DC). Two different experimental techniques were employed to assess the sensitivity of liner impedance to these configurations under varying grazing-flow velocities and SPLs.

The results suggest that the reactance is not significantly affected by perforation-edge geometry, given that this

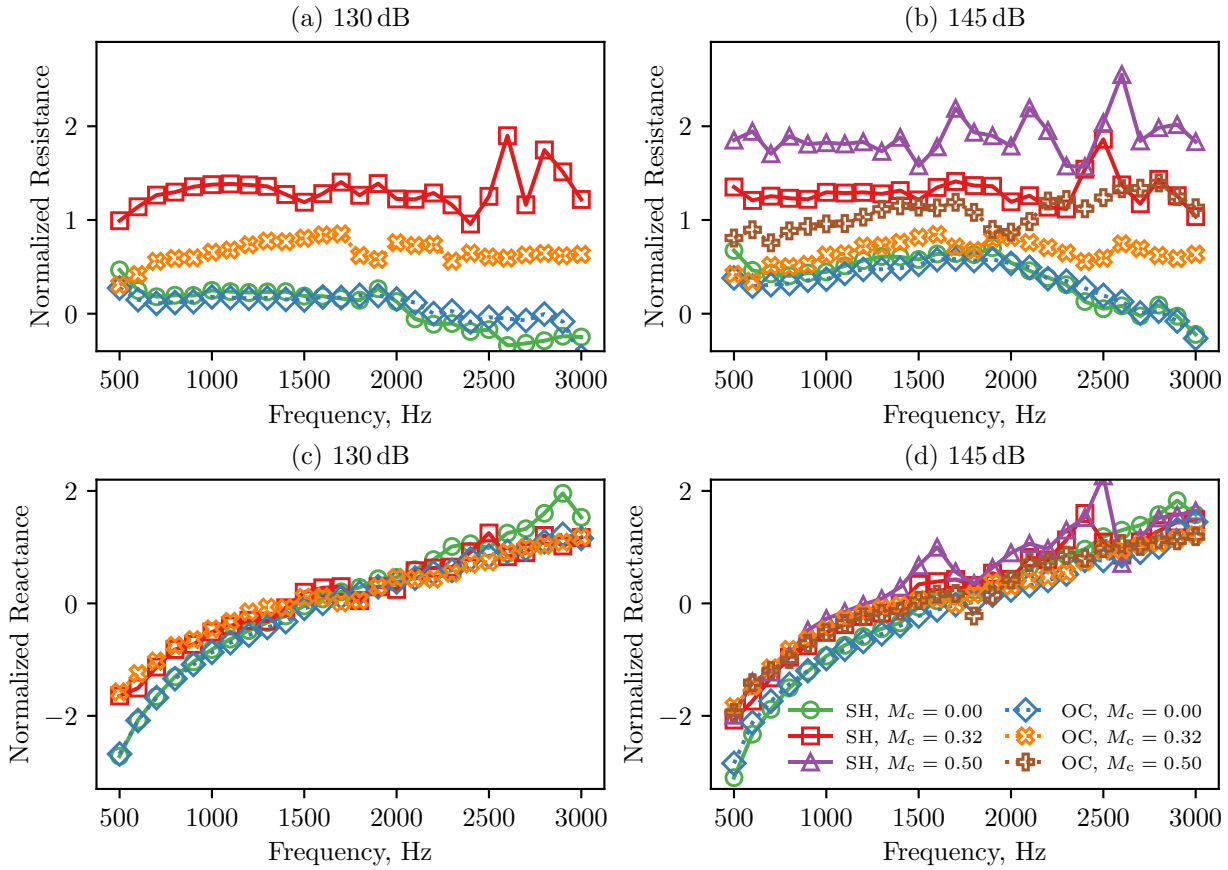


Fig. 8 Impedances obtained with the in-situ technique.

quantity is primarily governed by the overall liner cavities and bulk dimensions. In the absence of flow, it was observed that the presence of chamfers in the perforations can reduce the nonlinear resistance induced at high SPLs. There are still open questions regarding the fact that the presence of an internal chamfer leads to lower resistance than an external chamfer in some cases, and further investigation is left for future work.

In the presence of grazing flow, the nonlinear resistance induced by the flow dominates over the effects associated with SPL, and it was found that the presence of outer chamfers can lead to significantly lower resistance. This work aimed to help fill a gap in the literature by providing experimental data on the effects of chamfered edges on SDOF liner acoustic impedance, although some questions remain open. Furthermore, an analysis of the resistance ratios compared with a semi-empirical model revealed that the resistance drop for the outside-chamfered configuration scales accurately with predictions assuming a larger effective external diameter (i.e., an increased surface porosity). Nevertheless, it remains uncertain whether this reduction is strictly driven by the higher porosity or if it is a coincidental combination with the aerodynamic effects of the chamfer itself. Finally, future work will consider reducing the cavity height to extend the experimental evaluation to higher frequencies and further assess these geometric effects across a broader operating envelope. These questions may be addressed in future work by including conical holes, which would allow a gradual variation from the external to the internal diameter. Rounded edges should also be considered, as they would lead to smoother transitions between the internal and external diameters, although for the NIT it was found that edge rounding may lead to effects similar to those caused by chamfers [8]. Further studies may also include a parametric analysis of the POA and internal hole diameter, d_0.

Acknowledgments

F.R. Rossi and L.A. Bonomo gratefully acknowledge Luis Binotto and Danielle Fabri for their help in carrying out the experiments. This work was partially supported by the AeroAcoustics Research Consortium (AARC). The AARC

is a government-industry partnership supporting pre-competitive research for aircraft noise reduction. J. A. Cordioli acknowledges funding from the Brazilian funding agency CNPq (National Council for Scientific and Technological Development) through the process 315000/2021-0. The work of F. Avallone is co-funded by the European Union (ERC, LINING, 101075903). Views and opinions expressed are however those of the author(s) only and do not necessarily reflect those of the European Union or the European Research Council. Neither the European Union nor the granting authority can be held responsible for them.

References

[1] Smith, M. J. T., *Aircraft noise*, Cambridge University Press, UK, 1989.

[2] Paduano, A., Scarano, F., Cordioli, J., Casalino, D., and Avallone, F., "On the Impact of the Turbulent Grazing Flow Development on the Acoustic Response of an Acoustic Liner," Vol. 1035, 2026, p. A11. https://doi.org/10.1017/jfm.2026.11544.

[3] Guess, A. W., "Calculation of perforated plate liner parameters from specified acoustic resistance and reactance," *Journal of Sound and Vibration*, Vol. 40, No. 1, 1975, pp. 119–137. https://doi.org/10.1016/S0022-460X(75)80234-3.

[4] Yu, J., Ruiz, M., and Kwan, H. W., "Validation of Goodrich perforate liner impedance model using NASA langley test data," *14th AIAA/CEAS Aeroacoustics Conference (29th AIAA Aeroacoustics Conference)*, Vancouver, British Columbia, Canada, 2008. https://doi.org/10.2514/6.2008-2930.

[5] Cerizza, D., and Casalino, D., "An Indirect Impedance Eduction Process for Liners with Arbitrarily Complex Geometry," *AIAA AVIATION Forum*, American Institute of Aeronautics and Astronautics, San Diego, CA, USA, 2023. https://doi.org/10.2514/6.2023-4186.

[6] Murray, P., Ferrante, P., and Scofano, A., "Manufacturing process and boundary layer influences on perforate liner impedance," *11th AIAA/CEAS aeroacoustics conference*, American Institute of Aeronautics and Astronautics, Monterey, California, 2005. https://doi.org/10.2514/6.2005-2849.

[7] Quintino, N. T., Bonomo, L. A., Cordioli, J. A., Jones, M. G., Howerton, B. M., Nark, D. M., and Avallone, F., "Comparison of Impedance Eduction Test Rigs with Different Boundary-Layer Profiles," *AIAA Journal*, Vol. 63, No. 11, 2025, pp. 4872–4883. https://doi.org/10.2514/1.J065173.

[8] Avallone, F., Khedr, A., Paduano, A., Scarano, F., Meirelles, L., and Cordioli, J., "On the Relevance of Facesheet Orifice Geometry to Acoustic Liner Impedance," *npj Acoustics*, Vol. 2, No. 1, 2026, p. 6. https://doi.org/10.1038/s44384-026-00044-x.

[9] Serrano, P. G., Murray, P. B., and Astley, R. J., "Acoustic Impedance Measurements of Aerospace Resonators and High Fidelity Simulation of Non-Linear Interaction of Multiple Tones," *XII CONGRESSO/CONGRESO IBEROAMERICANO DE ACÚSTICA*, SOBRAC, Florianópolis, Brazil, 2022.

[10] Bonomo, L., Quintino, N., Spillere, A., Murray, P., and Cordioli, J., "A comparison of in situ and impedance eduction experimental techniques for acoustic liners with grazing flow and high sound pressure level," *International Journal of Aeroacoustics*, Vol. 23, 2024. https://doi.org/10.1177/1475472X231225629.

[11] Ingard, U., "Influence of Fluid Motion Past a Plane Boundary on Sound Reflection, Absorption, and Transmission," *The Journal of the Acoustical Society of America*, Vol. 31, 1959, pp. 1035–1036. https://doi.org/10.1121/1.1907805.

[12] Myers, M. K., "On the Acoustic Boundary Condition in the Presence of Flow," *Journal of Sound and Vibration*, Vol. 71, 1980, pp. 429–434. https://doi.org/10.1016/0022-460X(80)90424-1.

[13] Dokumaci, E., "Sound transmission in narrow pipes with superimposed uniform mean flow and acoustic modelling of automobile catalytic converters," *Journal of Sound and Vibration*, Vol. 182, No. 5, 1995, pp. 799 – 808. https://doi.org/10.1006/jsvi.1995.0233.

[14] Gabard, G., and Astley, R., "A computational mode-matching approach for sound propagation in three-dimensional ducts with flow," *Journal of Sound and Vibration*, Vol. 315, No. 4, 2008, pp. 1103 – 1124. https://doi.org/10.1016/j.jsv.2008.02.015.

[15] Levenberg, K., "A method for the solution of certain non-linear problems in least squares," *Quarterly of Applied Mathematics*, Vol. 2, No. 2, 1944, pp. 164–168. https://doi.org/10.1090/qam/10666.

[16] Marquardt, D. W., "An Algorithm for Least-Squares Estimation of Nonlinear Parameters," *Journal of the Society for Industrial and Applied Mathematics*, Vol. 11, No. 2, 1963, pp. 431–441. https://doi.org/10.1137/0111030.

[17] Dean, P., "An in situ method of wall acoustic impedance measurement in flow ducts," *Journal of Sound and Vibration*, Vol. 34, No. 1, 1974, pp. 97 – IN6. https://doi.org/10.1016/S0022-460X(74)80357-3.

[18] Ferrante, P., De Roeck, W., Desmet, W., and Magnino, N., "Back-to-back comparison of impedance measurement techniques applied to the characterization of aero-engine nacelle acoustic liners," *Applied Acoustics*, Vol. 105, 2016, pp. 129–142. https://doi.org/10.1016/j.apacoust.2015.12.004.

[19] Yang, J., Humbert, T., Golliard, J., and Gabard, G., "Shear flow effects in a 2D duct: Influence on wave propagation and direct impedance eduction," *Journal of Sound and Vibration*, Vol. 576, 2024, p. 118296. https://doi.org/10.1016/j.jsv.2024.118296.

[20] Bonomo, L. A., Brambley, E. J., and Cordioli, J. A., "Effects of the sheared flow velocity profile on impedance eduction in a 2D duct," *Acta Acustica*, Vol. 10, 2026, p. 6. https://doi.org/10.1051/aacus/2026005.

[21] Bonomo, L. A., Quintino, N. T., Spillere, A. M. N., Murray, P. B., and Cordioli, J. A., "A comparison of in situ and impedance eduction experimental techniques for acoustic liners with grazing flow and high sound pressure level," *International Journal of Aeroacoustics*, 2024, p. 1475472X231225629. https://doi.org/10.1177/1475472X231225629.